

In-Plane Electric-Field-Induced Orbital Hybridization of Excitonic States in Monolayer WSe₂


Bairen Zhu,^{1,*} Ke Xiao,^{2,*} Siyuan Yang,² Kenji Watanabe,³ Takashi Taniguchi,⁴ and Xiaodong Cui^{2,‡}

¹Key Laboratory of Quantum Precision Measurement of Zhejiang Province, Department of Applied Physics, Zhejiang University of Technology, Hangzhou 310023, China

²Physics Department, University of Hong Kong, Hong Kong, China

³Research Center for Functional Materials, National Institute for Materials Science, 1-1 Namiki, Tsukuba 305-0044, Japan

⁴International Center for Materials Nanoarchitectonics, National Institute for Materials Science, 1-1 Namiki, Tsukuba 305-0044, Japan

 (Received 7 October 2021; revised 6 May 2023; accepted 6 June 2023; published 17 July 2023)

The giant exciton binding energy and the richness of degrees of freedom make monolayer transition metal dichalcogenide an unprecedented playground for exploring exciton physics in 2D systems. Thanks to the well-energetically separated excitonic states, the response of the discrete excitonic states to the electric field could be precisely examined. Here we utilize the photocurrent spectroscopy to probe excitonic states under a static in-plane electric field. We demonstrate that the in-plane electric field leads to a significant orbital hybridization of Rydberg excitonic states with different angular momentum (especially orbital hybridization of $2s$ and $2p$) and, consequently, optically activates $2p$ -state exciton. Besides, the electric-field controlled mixing of the high lying exciton state and continuum band enhances the oscillator strength of the discrete excited exciton states. This electric field modulation of the excitonic states in monolayer TMDs provides a paradigm of the manipulation of 2D excitons for potential applications of the electro-optical modulation in 2D semiconductors.

DOI: [10.1103/PhysRevLett.131.036901](https://doi.org/10.1103/PhysRevLett.131.036901)

Hybridization primitively indicates a mixing of atomic orbitals of comparable energies for the description of chemical bonds in valence band theory. In 2D TMDs, band edges around the $\pm K$ valleys are primarily constructed by d orbitals of transition-metal atoms with a small component of p orbitals of chalcogen atoms due to atomic orbital hybridization [1–3]. This atomic orbital hybridization leads to a significant spin-orbit coupling in the conduction band edge [2]. Orbital hybridization of valley excitons exists not only among atomic orbitals but also in excitonic orbitals. For valley excitons in monolayer TMDs, the complete wave function is described with the direct product of electron or hole's Bloch functions featured with parent atomic orbitals and envelope functions featured with excitonic orbitals. The envelope functions denote the relative motions between electron and hole and could be described with a Rydberg notation (n, l) , where n, l are the principal index ($n = 1, 2, 3, \dots$) and orbital angular momentum quantum number ($l = 0, 1, 2, \dots$), respectively. The different Rydberg excitonic orbitals have the distinct optical properties, in an over-simplified manner, either bright or dark. The bright excitons denote the optically active excitons associated with the dipole allowed one-photon transition, which dominates the linear optical properties. They are usually with an s -state exciton envelope function with zero orbital angular momentum ($l = 0$). However, their excited states are not necessarily

bright. For example, $2p, 3p, \dots$ -state excitons are naturally considered as the angular-momentum forbidden dark excitons owing to the symmetry of the envelope function in the standard 2D exciton model [4–7]. In monolayer TMDs, the threefold in-plane rotational symmetry from the crystal lattice renders p -state excitons bright with the microscopic mechanism of the trigonal warping effect [8]. However, the p -state excitons are absent in the experimental linear optical spectra [9–11] and the calculations [8,12] attribute the dark p -state excitons to the negligible oscillator strength in one-photon (dipole allowed) transition. Recently, there are several theoretical proposals that disorders, Rashba spin-orbit interaction, or skyrmions could brighten p -state excitons [13,14].

Here we demonstrate an electric-field controlled excitonic orbital hybridization in h BN-encapsulated monolayer WSe₂ with the linear photocurrent spectroscopy. We observe that an in-plane electric field could break the rotational symmetry of exciton envelope functions and induce a significant orbital hybridization of Rydberg excitons with different angular momentum by mixing their envelope functions and consequently brighten the $2p$ -state exciton. Besides, the hybridization between high lying excitons and the continuum band enhances the oscillator strength of the discrete exciton states. Our experiments unambiguously demonstrate that the energy, linewidth, and the oscillator strength of the hybrid exciton states could be

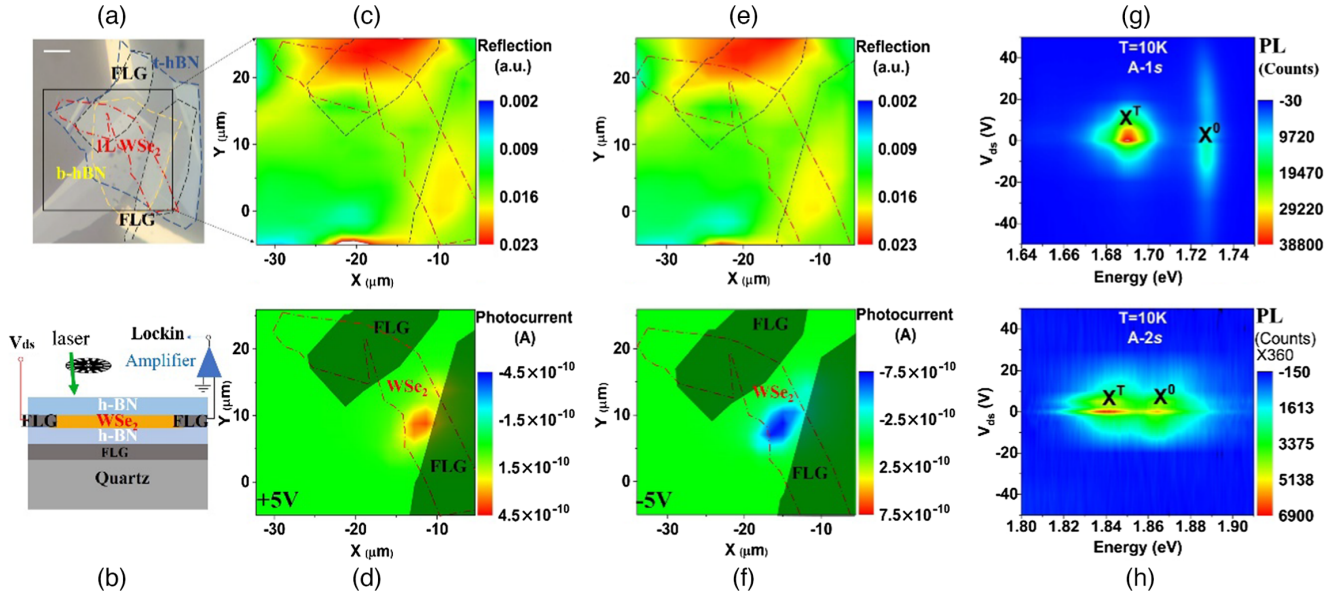


FIG. 1. (a) Optical microscopic image of the *h*BN-encapsulated monolayer WSe₂ with few-layer graphene (FLG) as electric contacts. The different layers are marked by dashed lines of different colors. The white scale bar is 5 μ m. (b) Schematic of the device on a transparent quartz substrate for the photocurrent measurement. (c)–(d) The reflection and photocurrent mappings of the device at $V_{ds} = +5$ V and $T = 10$ K. The scanning range covers the marked area in (a). Two electric contacts of FLG and 1L-WSe₂ are also labeled for reference. (e)–(f) The reflection and photocurrent mappings at $V_{ds} = -5$ V. Photoluminescence of the A-1s exciton (g) and A-2s exciton (h) on the spot where the photocurrent is taken as a function of the source-drain voltage at $T = 10$ K. The fake colors in these mappings present the signal magnitude with the linear spectra scales where the minimum starts from blue to red at maximum.

efficiently modulated with an in-plane electric field owing to the unique character of 2D excitons.

The device is made of *h*BN-encapsulated monolayer WSe₂ with few-layer graphene as electric contacts. To avoid the photogating effect from substrates, we transfer the device onto transparent fused quartz substrates, as shown in Fig. 1(a). The excitation beam is focused through a scanning objective onto a spot of ~ 1 micron on the device. Excitons are dissociated by the local electric field and a photocurrent is collected via a lock-in technique [Fig. 1(b)]. Figures 1(c) and 1(d) show the representative reflection and photocurrent maps under $V_{ds} = +5$ V excited by a 2.4 eV laser source at $T = 10$ K. The photocurrent arises at the region adjacent to the electric contact where the local electric field is expected to be maximum and strong enough to ionize excitons.

The local carrier density is investigated by the 2D color map of low-temperature photoluminescence (PL) as a function of the source-drain bias from -50 to $+50$ V. Figure 1(g) shows that the PL map of the ground state band edge exciton A-1s (which denotes the ground 1s state of the band edge A exciton) and its corresponding trions peak around $V_{ds} = 0$ V. The trions consisting of two electron-charged trions, namely, intervalley and intravalley trions, signal the weak electron doping at zero bias. The PL peaks redshift away from the zero-bias state, and fade with the increasing source-drain bias in both negative and positive directions. These phenomena are significantly different

from those in the electric gated PL experiments, where the increased carrier density transfers the oscillator strength from neutral excitons to trions and shifts the energy of the neutral excitons and trions in opposite directions, as described with the Fermi-polaron model [15–17]. This in-plane modulated PL experiment reveals the in-plane electric field in force without noticeable doping effect. The suppressed PL emission at the increased bias implies the exciton dissociation under external electric field. The A-1s trions fade at lower electric field than that of A-1s neutral excitons, and it is attributed to the small binding energies of the trions. The redshift of both neutral excitons and trions with the increased electric field could be regarded as the excitonic dc Stark effect [18,19]. The similar electric field dependent PL behaviors occur in A-2s excitons [Fig. 1(h)] with a higher sensitivity to the in-plane electric field. The PL intensities of both neutral A-2s excitons and the related trions drop to an undetectable level under the bias beyond $V_{ds} = \pm 10$ V, as a result of weaker exciton binding energies. Obviously, the PL spectroscopy of Rydberg excitons is not capable of tracing the effect of in-plane electric field.

We record the reflectance contrast and photocurrent spectra of the *h*BN-encapsulated monolayer WSe₂ by the excitation energy or wavelength with an intensity below 0.5 μ W. Figure 2(a) depicts the reflectance contrast and the photocurrent at $V_{ds} = +2$ V as a function of the excitation energy. The band edge ground state exciton

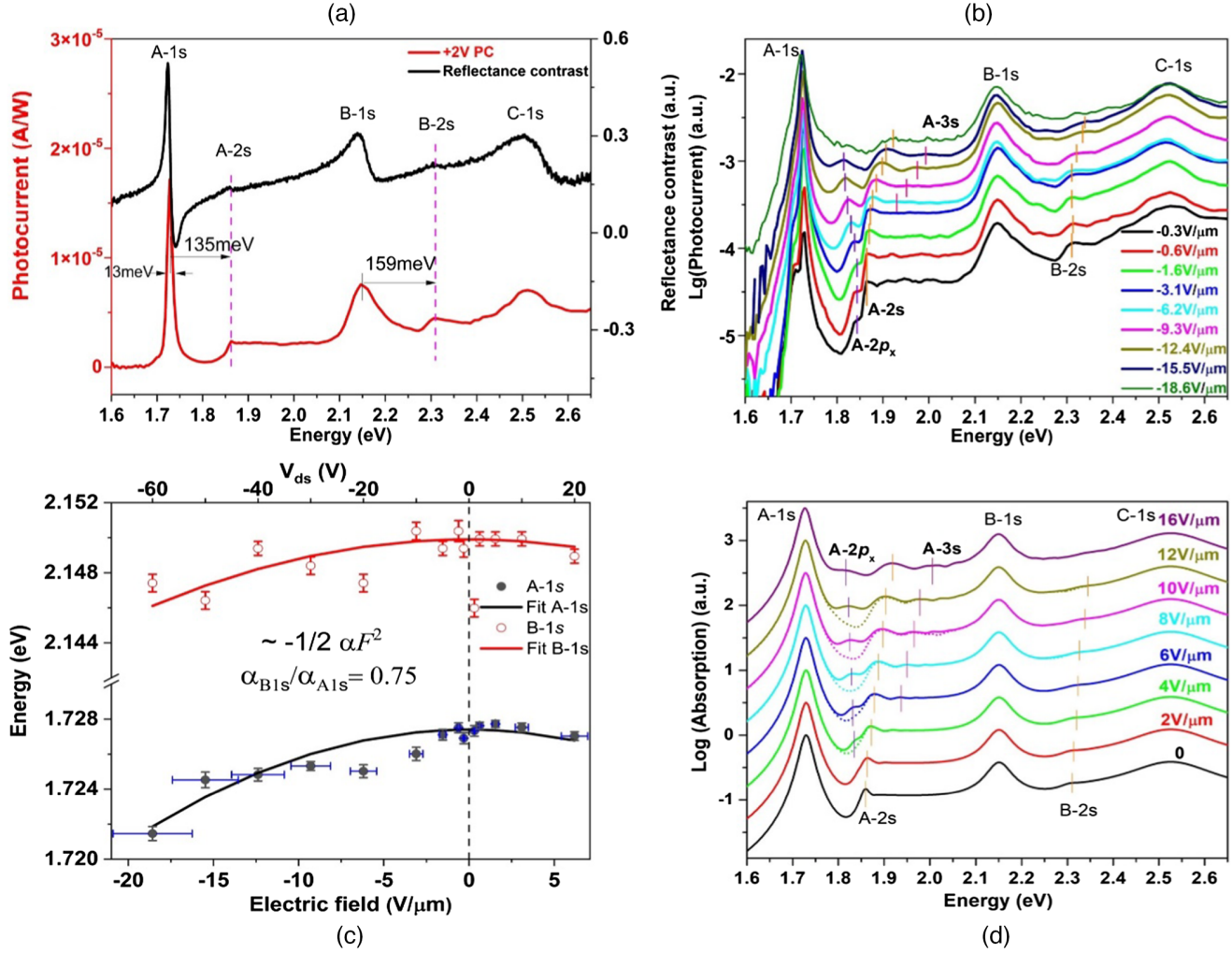


FIG. 2. (a) Reflectance contrast and photocurrent spectra at $V_{ds} = +2$ V of h BN-encapsulated monolayer WSe_2 devices. (b) Photocurrent spectra on a log scale under various in-plane electric fields that are extracted by excitonic dc stark effect of A-1s exciton. Enlargement of the shifts of A1s and the data under the positive electric field and are shown in Supplemental Material, Sec. 2 [22]. (c) The energy shift of the 1s exciton is proportional to the square of electric field F and exciton in-plane polarizability α ($\sim -1/2\alpha F^2$) with the fitting error bar of energy. The in-plane electric fields are extracted with a h -BN dielectric constant $\epsilon_{BN} = 4.5$. The error bars of electric fields result from the uncertainty in the h -BN dielectric constant ϵ_{BN} (3.0–4.5). The inhomogeneity of in-plane electric field owing to the sample or substrate inhomogeneity is shown in Supplemental Material, Sec. 3 [22]. The in-plane polarizability of the B exciton is found to be smaller than that of the A exciton, implying a larger exciton binding energy owing to the larger effective mass. Similar data from other devices are presented in Supplemental Material, Sec. 4 [22]. (d) The calculated electroabsorption of 1L WSe_2 on a log scale from 0 to 16 $V/\mu m$, consistent with the experimental results in (b). The dashed lines denote the electroabsorption spectra without the $2p$ state.

$A-1s$, the ground state spin-off exciton $B-1s$, and the excitons around the Γ point of the Brillouin zone $C-1s$ exciton are clearly observed in both spectra. The phenomenon is consistent with the previous photocurrent report [18,20]. A significant feature of the photocurrent spectra is the enhanced weight of the excited-state excitons including $A-2s$ and $B-2s$, which were previously ignored in the previous photocurrent measurements [18,20]. Although the occupation of these excited state is much less than the ground states, the weaker binding energy leads to a much higher ionization rate as the electron-hole tunneling

is the dominating mechanism for exciton ionization in monolayer TMDs [20,21] (see Supplemental Material, Sec. 1 [22]). So, it is advantageous to study the excited exciton states with photocurrent spectroscopy.

Figure 2(a) shows that the excited-state excitons $A-2s$ and $B-2s$ lie at 135 and 159 meV above their corresponding ground-state excitons $A-1s$ and $B-1s$, respectively. It hints that the binding energy of B excitons is larger than that of the A exciton. In the photocurrent spectrum, the $A-2s$ exciton appears at the starting point of a steplike feature and it may result from a $A-2s$ exciton state merging into the

onset of the interband continuum. Figure 2(b) depicts the photocurrent spectra on a log scale as a function of the applied source-drain bias from -1 to -60 V that can be converted to the electric field from -0.3 to -18.6 V/ μm in the following paragraph. Both $A-1s$ and $B-1s$ excitons energetically redshift with the increasing in-plane electric field as a result of the excitonic dc Stark effect and are well fitted in a quadratic relationship $\sim \Delta E = -\frac{1}{2}\alpha F^2$, where α is the in-plane polarizability, that of $A-1s$ is estimated to be around 2×10^{-17} em^2/V with the dielectric constants of $\text{hBN} = 4.5$ [18]. Therefore, we could directly extract the magnitude of the in-plane electric field instead of displacement field. Given the uncertainty and inhomogeneity of the dielectric constant of the h-BN flakes (in the range of 3.0–4.5) [11,23–29], error bars are provided to give a limit of the electric fields, as shown in Fig. 2(c). Besides, we extract the in-plane polarizability of the $B-1s$ exciton of $0.75\alpha_A$ and it concludes that the exciton binding energy of $B-1s$ exciton is 1.33 times that of $A-1s$ exciton [30], which is consistent with the aforementioned energy difference of $A-2s/B-2s$ [Fig. 2(a)] and the previous report on a larger effective mass [3,31]. The photocurrent signal below $A-1s$ exciton (labeled as trion) totally disappears when V_{ds} is beyond -10 V (equivalent to $F = -3.1$ V/ μm) since the trions cannot survive under a large electric field, as demonstrated in the electric field dependent PL spectra [Fig. 1(g)].

We also observe two excited exciton states in the vicinity of the $A-2s$ state, which could not be identified directly. We could exclude the possibility of the $A-2s$ trion state for three reasons. First, the aforementioned PL measurement shows that the source-drain voltage generates an in-plane electric field with negligible doping effect. Second, throughout the range of electric field where the PL of the $A-2s$ trion can be probed, the energy of the $A-2s$ trion has an unresolved shift whereas this peak in the photocurrent spectra redshifts by a few meV (Supplemental Material, Sec. 5 [22]). Third, the trion state of $A-1s$ is negligible in the photocurrent experiments under a sizable in-plane electric field. So the trion state of a much-weaker-oscillator-strength $A-2s$ is unlikely to be prominent in photocurrent spectra. Figure 2(d) shows the calculated electroabsorption spectra can mostly reproduce all features including two unidentified peaks from experimental photocurrent spectra. According to the detailed analysis of calculated electroabsorption spectra, we assign them to $2p_x$ (x denotes the direction of in-plane electric field) and $3s$ states, which is elaborated in the following section.

From the classical dipole model of neutral exciton, there exists a critical field by simply evaluating $F_c = [E_b/(er)]$ (E_b , e , r are the exciton binding energy, electron charge, and Bohr radius, respectively) for fully dissociation of Rydberg excitons in monolayer WSe_2 (Supplemental Material, Sec. 6 [22]) [11,32,33]. The actual in-plane electric field with the order of 5 V/ μm is perturbative to $1s$ exciton while it may be strong enough to ionize excitons with higher principal

quantum number ($n \geq 3$). Meanwhile, the electric field of 5 V/ μm is comparable to the critical field for the excited excitons ($n = 2$) that include nondegenerate states consisting of $2s$, $2p_{\pm}$ excitons with valley degeneracy of two in monolayer TMDs. Therefore, these excitonic states will be influenced enormously based on these assumptions.

To accurately model the exciton energy under an external electric field, we numerically solve the Mott-Wannier exciton model to obtain the eigenenergies and eigenwave functions of Rydberg excitons, the effective Hamiltonian reads

$$\left\{ -\frac{\hbar^2}{2\mu} \nabla^2 + w(r) + e\vec{F} \cdot \vec{r} \right\} \Psi = E\Psi,$$

where the $w(r) = -(e^2/8\epsilon_0 r_0)[H_0(\kappa r/r_0) - Y_0(\kappa r/r_0)]$ is the Rytova-Keldysh potential describing the screening

Coulomb attraction in the 2D case, μ , $e\vec{F} \cdot \vec{r}$ represent exciton effective mass and the external electric field term, respectively. The absorption spectra are then calculated as $\omega \text{Im}[\chi(\omega)]$. (See more details in Supplemental Material, Sec. 7 [22]) [20,34,35].

We trace the two unidentified peaks under the different in-plane electric fields mentioned in the last section. By calculating the projection of these corresponding eigenfunctions $|\phi\rangle$ on the excitonic states (to distinguish excitonic states whether they are under an in-plane electric field, we define the original excitonic states without electric field by the superscript 0, such as $|1s^0\rangle$, $|2p_x^0\rangle$, $|2s^0\rangle$...), we find that the two peaks mainly consist of the $2p_x$ and $3s$ states, respectively, and then we can safely assign them to $2p_x$ and $3s$ excitonic states (more details in Supplemental Material, Sec. 8 [22]).

Figure 3(a) shows the real space distributions of $1s$, $2p_x$, $2p_y$, $2s$ states at various representative electric fields, and Figs. 3(b)–3(e) summarize the dominated orbital compositions of these states. According to the electric field effect on excitons, we describe the scenario exclusively in three regions I, II, III for low, medium, and high electric field, respectively. Under low electric field, $e\vec{F} \cdot \vec{r} \ll w(r)$, the external field is perturbative on the excitonic states so that these states almost preserve as original ones. The spatial distributions of these four envelope wave functions almost keep unchanged, as demonstrated in region I [the blue frame of Fig. 3(a)] and the original states keep a major component (more than 90%) in the blue region I of Figs. 3(b)–3(e). In the region II of medium electric field, we can further divide it into region IIa, $e\vec{F} \cdot \vec{r} < w(r)$, and region IIb, $e\vec{F} \cdot \vec{r} > w(r)$. In region IIa, the eigenstates are still discrete excitonic states and the spatial distributions of exciton wave functions show a noticeable distortion from the original ones [the pink frame of Fig. 3(a)]. This is because that the excitonic states start to hybridize with

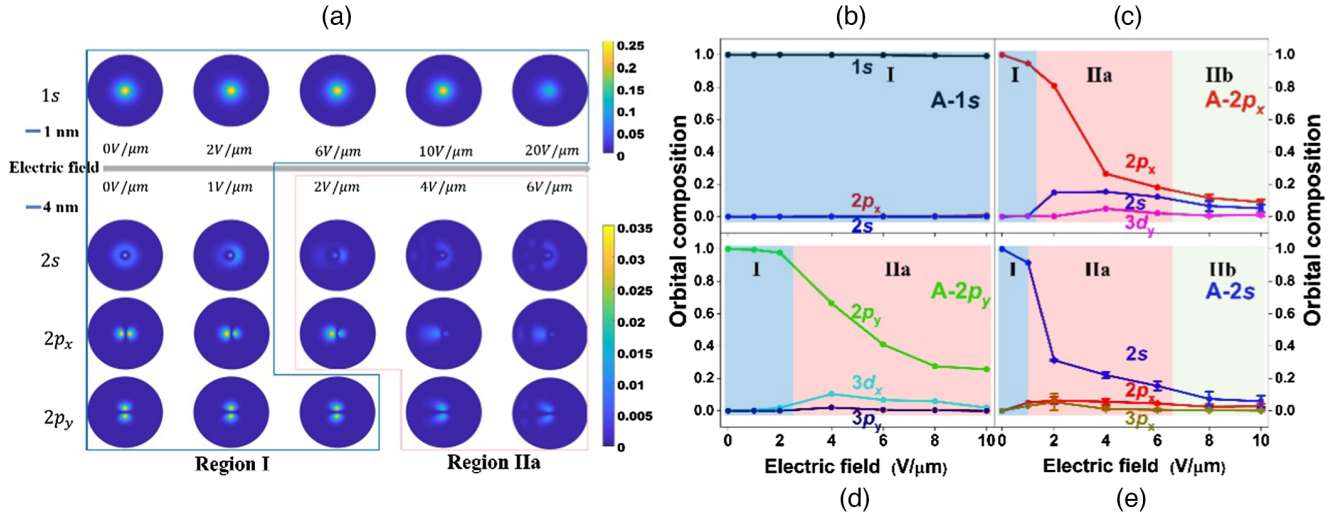


FIG. 3. (a) The spatial distribution of excitonic envelope wave function with different orbitals and envelope functions as a function of the in-plane electric field. In region I marked in blue, all exciton states preserve without significant change. The $1s$ state keeps unchanged until $F = 20$ V/ μm . In region IIa marked in pink, $2p_x$, $2p_y$, and $2s$ states distort evidently owing to the orbital hybridization with some neighboring states. (b)–(e) The analysis of the orbital composition of hybrid excitons as a function of in-plane electric field. The error bar denotes the state energy broadening.

some adjacent ones to non-negligible extent, forming hybrid excitons. The $2s/2p_x$ state still keeps the dominant component despite of a large reduction in the hybrid exciton shown as the pink region IIa of Figs. 3(b)–3(e). $2p_y$ state is relatively immune to the orthogonal electric field (x -direction). Here, the dark $2p_x$ state transits from dark to bright state and emerges in the linear photocurrent spectrum as it effectively hybridizes with the bright $2s$ state [Fig. 3(c)]. The bright $2s$ state hybridizes with the dark $2p_x$ state at the increase of electric field [Fig. 3(e)]. Note that the dark $2p_y$ state does not hybridize with the $2s$ state, but mixes with the dark $3d_x$ state [Fig. 3(d)]. Therefore, it keeps dark and undetectable. In region IIb, $e\vec{F} \cdot \vec{r} > w(r)$, the eigenstates carry similar features as the continuous functions from 2D Airy equation $[-(\hbar^2/2\mu)\nabla^2 + e\vec{F} \cdot \vec{r}]\Psi = E\Psi$. Namely, the hybrid excitons mix with the continuous states, leading to effective inhomogeneous broadening so that they become a broad rather than discrete distribution in energy spectrum, denoted as error bars in Figs. 3(b)–3(e). Here, we confirm the linewidths of $2s$ or $2p_x$ become broader from $F = 6$ V/ μm in the photocurrent experiment [Fig. 2(b)], although the $2s$ or $2p_x$ component in the hybrid excitons decreases but still gives the major contribution. In the region III, $e\vec{F} \cdot \vec{r} \gg w(r)$, the screening Coulomb attraction can be considered as a perturbative term of the two-dimensional Airy equation where the eigenstates are mostly continuous. We do not reach so large electric field of the region III in our experiments.

In summary, threefold in-plane rotational symmetry could theoretically mix the s - p excitonic states, but the mixing strength is expected to be too small to brighten the

$2p$ state [8,12]. In our case, the applied in-plane electric field is orders of magnitude smaller than the crystal field, but large enough to break the in-plane rotational symmetry of the $n = 2$ exciton envelope function. Consequently, the angular momentum is not well defined and the wave functions of $2s$ and $2p$ states are hybridized if the electric field is comparable to the exciton critical field. The dipole-forbidden (dark) A - $2p_x$ excitonic state could be brightened by an in-plane electric field in the linear spectra due to the orbital hybridization with the $2s$ state. It is further confirmed by the simulated absorption spectrum calibrated with the experimental data, as shown in Fig. 2(d).

The $3s$ state is predicted to undergo an orbital hybridization with the dark $3p_x$ and $3d_y$ states under a small electric field. However, we could not observe the $3s$ state under the electric field ranging from zero until $F = -3.1$ V/ μm presumably owing to its weak oscillator strength and the signal-noise ratio of the experiment setup. The $3s$ state clearly emerges under the electric field from -6.2 to -15.5 V/ μm in the photocurrent spectra [Fig. 2(b)]. We attribute the enhancement of $3s$ state to the hybridization with the continuous states. (See Supplemental Material, Sec. 9 [22]).

The increase of exciton orbital hybridization is followed by the energy shifts of the hybrid excitons. We record the energy values of hybrid excitons A - $1s$, $2s$, $2p_x$, $3s$, and B - $1s$, $2s$ from both photocurrent experiments (dots) and the numerical calculation (solid lines, $\mu = 0.23m_e$, $\kappa = 4.5$, $r_0 = 4.62$ nm Supplemental Material, Sec. 7 [22]) shown in Fig. 4—they are very well consistent. The $1s$ exciton experiences a small quadratic redshift with the electric field owing to the negligible orbital hybridization of the $2p_x$

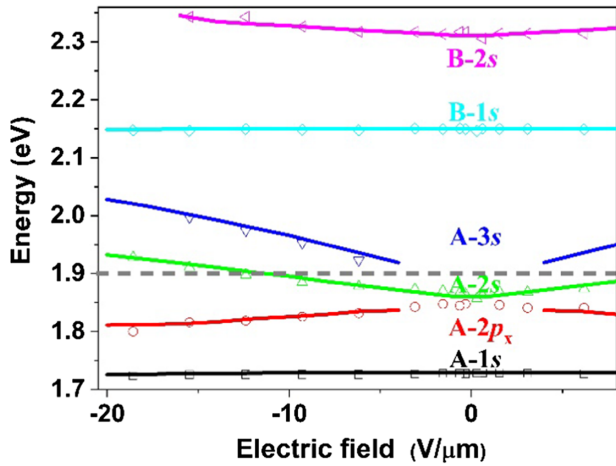


FIG. 4. Energies of hybrid excitons from experimental photocurrent spectra (dots) and calculated electroabsorption (solid lines), respectively.

state at $F = -18.6$ V/ μm [Fig. 2(c)]. In contrast, the $2p_x$ redshifts while $2s$ and $3s$ blueshift by tens of meV when in-plane electric field goes to 16 V/ μm . The $2p_x$ exciton effectively hybridizes with $2s$ state while little with the $3d_y$ state. Although it is difficult to resolve $A-3s$ exciton under small electric fields in our experiment, its energy shift under electric fields $F = -6.2 \sim -15.5$ V/ μm is well consistent with the numerical values. In particular, the energies of $A-2s$ and $3s$ excitons under a fairly strong in-plane electric field could exceed that of the continuous band (1.90 eV), denoted as gray dashed line in Fig. 4. This does not mean the exciton binding energy is positive. As the hybrid exciton gains extra electric potential energy from the external electric field, the exciton binding energy is still negative, which secures these exciton states in the photocurrent spectrum (see Supplemental Material, Sec. 10 [22]).

In conclusion, the in-plane electric field breaks the in-plane rotational symmetry of the exciton envelope functions and mixes exciton states with different excitonic orbitals, resulting in the formation of new hybrid excitons. We demonstrate that the energy, linewidth, and oscillator strength of the hybrid excitons can be electrically tuned by the in-plane electric field with the magnitude of 1–16 V/ μm . The $2s$ and $2p_x$ excitons can hybridize each other efficiently and this hybridization optically activates the dark $2p_x$ exciton in the one-photon photocurrent spectrum. Besides, the oscillator strength of the $3s$ exciton is promoted due to its hybridization with the continuum band. Also, we observe that the in-plane polarizability of the $B-1s$ exciton is smaller than that of $A-1s$ and the energy separation between $2s$ and $1s$ of the B exciton is larger than that of the A exciton, both implying the higher binding energy of the B exciton. Besides, the hybrid excitons under an in-plane electric field inherit the properties of all base orbitals, and, consequently, they may be bright in both one-photon and two-photon optical transitions. Our results demonstrate the exceptional electric tunability of 2D

excitons, providing a potential application of electro-optical modulations with 2D TMDs.

The work was supported by the National Natural Science Foundation of China (No. 12104399) and the Hong Kong University Grants Council/Research grants council under schemes of (AoE/P-701/20), General Research Fund (GRF) (17300520), and Collaborative Research Fund (CRF) (C7036-17W), National Key R&D Program of China (2020YFA0309600), and Guangdong-Hong Kong Joint Laboratory of Quantum Matter. K. W. and T. T. acknowledge support from the Elemental Strategy Initiative conducted by the MEXT, Japan (Grant No. JPMXP0112101001) and JSPS KAKENHI (Grants No. 19H05790 and No. JP20H00354).

*These authors contributed equally to this work.

†zhubair@zjut.edu.cn

‡xdcui@hku.hk

- [1] G.-B. Liu, W.-Y. Shan, Y. Yao, W. Yao, and D. Xiao, *Phys. Rev. B* **88**, 085433 (2013).
- [2] K. Kořmider, J. W. Gonzalez, and J. Fernandez-Rossier, *Phys. Rev. B* **88**, 245436 (2013).
- [3] A. Kormanyos, G. Burkard, M. Gmitra, J. Fabian, V. Zolyomi, N. D. Drummond, and V. Fal’ko, *2D Mater.* **2**, 022001 (2015).
- [4] Z. Ye, T. Cao, K. O’Brien, H. Zhu, X. Yin, Y. Wang, S. G. Louie, and X. Zhang, *Nature (London)* **513**, 214 (2014).
- [5] K. He, N. Kumar, L. Zhao, Z. Wang, K. F. Mak, H. Zhao, and J. Shan, *Phys. Rev. Lett.* **113**, 026803 (2014).
- [6] B. Zhu, X. Chen, and X. Cui, *Sci. Rep.* **5**, 9218 (2015).
- [7] G. Wang, X. Marie, I. Gerber, T. Amand, D. Lagarde, L. Bouet, M. Vidal, A. Balocchi, and B. Urbaszek, *Phys. Rev. Lett.* **114**, 097403 (2015).
- [8] P. Gong, H. Yu, Y. Wang, and W. Yao, *Phys. Rev. B* **95**, 125420 (2017).
- [9] A. Chernikov, T. C. Berkelbach, H. M. Hill, A. Rigosi, Y. Li, O. B. Aslan, D. R. Reichman, M. S. Hybertsen, and T. F. Heinz, *Phys. Rev. Lett.* **113**, 076802 (2014).
- [10] G. Wang, A. Chernikov, M. M. Glazov, T. F. Heinz, X. Marie, T. Amand, and B. Urbaszek, *Rev. Mod. Phys.* **90**, 021001 (2018).
- [11] A. V. Stier, N. P. Wilson, K. A. Velizhanin, J. Kono, X. Xu, and S. A. Crooker, *Phys. Rev. Lett.* **120**, 057405 (2018).
- [12] M. M. Glazov, L. E. Golub, G. Wang, X. Marie, T. Amand, and B. Urbaszek, *Phys. Rev. B* **95**, 035311 (2017).
- [13] G. Berghauser, A. Knorr, and E. Malic, *2D Mater.* **4**, 015029 (2016).
- [14] L. Chirrolli, *Phys. Rev. B* **101**, 075426 (2020).
- [15] M. Sidler, P. Back, O. Cotlet, A. Srivastava, T. Fink, M. Kroner, E. Demler, and A. Imamoglu, *Nat. Phys.* **13**, 255 (2017).
- [16] D. K. Efimkin and A. H. MacDonald, *Phys. Rev. B* **95**, 035417 (2017).
- [17] K. Xiao, T. Yan, Q. Liu, S. Yang, C. Kan, R. Duan, Z. Liu, and X. Cui, *J. Phys. Chem. Lett.* **12**, 2555 (2021).
- [18] T. G. Pedersen, *Phys. Rev. B* **94**, 125424 (2016).

- [19] I. Verzhbitskiy, D. Vella, K. Watanabe, T. Taniguchi, and G. Eda, *ACS Nano* **13**, 3218 (2019).
- [20] M. Massicotte *et al.*, *Nat. Commun.* **9**, 1633 (2018).
- [21] S. Haastrup, S. Latini, K. Bolotin, and K. S. Thygesen, *Phys. Rev. B* **94**, 041401(R) (2016).
- [22] See Supplemental Material at <http://link.aps.org/supplemental/10.1103/PhysRevLett.131.036901> for methods, tunneling ionization rates of Rydberg excitons, photocurrent spectra at positive voltage, the inhomogeneity of in-plane electric field in the device, repeatability of the photocurrent results from other devices, excluding the possibility of the peak below $A-2s$ as trion state, the estimated critical electric field of Rydberg excitons, calculated electro-absorption spectra under in-plane electric field, calculation of the components of $1s$, $2s$, ... in the new hybrid states under in-plane electric field, $3s$ state under in-plane electric field, calculation of the electric potential, binding energy of hybrid excitons under in-plane electric field, which includes Refs. [11,20,32–35].
- [23] C. R. Dean *et al.*, *Nat. Nanotechnol.* **5**, 722 (2010).
- [24] A. Laturia, M. L. Van de Put, and W. G. Vandenberghe, *npj 2D Mater. Appl.* **2**, 6 (2018).
- [25] M. Goryca *et al.*, *Nat. Commun.* **10**, 4172 (2019).
- [26] H. Polshyn *et al.*, *Nature (London)* **588**, 66 (2020).
- [27] E. C. Regan *et al.*, *Nature (London)* **579**, 359 (2020).
- [28] X. Wang *et al.*, *Nat. Nanotechnol.* **16**, 1208 (2021).
- [29] J. Gu, L. Ma, S. Liu, K. Watanabe, T. Taniguchi, J. C. Hone, J. Shan, and K. F. Mak, *Nat. Phys.* **18**, 395 (2022).
- [30] B. Scharf, T. Frank, M. Gmitra, J. Fabian, I. Žutić, and V. Perebeinos, *Phys. Rev. B* **94**, 245434 (2016).
- [31] H. M. Hill, A. F. Rigosi, C. Roquelet, A. Chernikov, T. C. Berkelbach, D. R. Reichman, M. S. Hybertsen, L. E. Brus, and T. F. Heinz, *Nano Lett.* **15**, 2992 (2015).
- [32] S.-Y. Chen *et al.*, *Nano Lett.* **19**, 2464 (2019).
- [33] E. Liu, J. van Baren, T. Taniguchi, K. Watanabe, Y.-C. Chang, and C. H. Lui, *Phys. Rev. B* **99**, 205420 (2019).
- [34] T. C. Berkelbach, M. S. Hybertsen, and D. R. Reichman, *Phys. Rev. B* **88**, 045318 (2013).
- [35] F. A. Rasmussen and K. S. Thygesen, *J. Phys. Chem. C* **119**, 13169 (2015).